Journal of Hydrology 646 (2025) 132322

Contents lists available at ScienceDirect

Journal of Hydrology

journal homepage: www.elsevier.com/locate/jhydrol

Research papers

Groundwater flow and salinity dynamics in swash Zones: Combined effects of Evaporation, Waves, and geologic heterogeneity

Xiaolong Geng [a,b,*], Holly A. Michael [c,d], James W. Heiss [e], Michel C. Boufadel [f], Hailong Li [g], Yan Zhang [h]

[a] Department of Earth Sciences, University of Hawai'i at Mānoa, Honolulu, HI 96822, USA
[b] Water Resources Research Center, University of Hawai'i at Mānoa, Honolulu, HI 96822, USA
[c] Department of Earth Sciences, University of Delaware, Newark, DE 19716, USA
[d] Department of Civil and Environmental Engineering, University of Delaware, Newark, DE 19716, USA
[e] Department of Environmental, Earth, and Atmospheric Sciences, University of Massachusetts Lowell, Lowell, MA 01854, USA
[f] Department of Civil and Environmental Engineering, New Jersey Institute of Technology, University Heights, Newark, NJ 07102, USA
[g] State Environmental Protection Key Laboratory of Integrated Surface Water-Groundwater Pollution Control, School of Environmental Science & Engineering, Southern University of Science and Technology, Shenzhen 518055, China
[h] MOE Key Laboratory of Groundwater Circulation & Environment Evolution, School of Water Resources and Environment, China University of Geosciences (Beijing), Beijing 100083, China

ARTICLE INFO

This manuscript was handled by Corrado Corradini, Editor-in-Chief, with the assistance of Eddie Banks, Associate Editor

ABSTRACT

This study employs groundwater simulations to examine the combined effects of waves, evaporation, and geologic heterogeneity on the flow and salinity dynamics in a shallow beach environment. The modeling results reveal that wave motion generates a saline plume beneath the swash zone, with hypersalinity near the surface triggered by evaporation. Geologic heterogeneity critically controls the temporal and spatial patterns of evaporation, moisture content, and salinity in the swash zone. Heterogeneous capillarity creates localized moisture hotspots within the unsaturated zone, which support enhanced evaporation and therefore facilitate salt accumulation at the surface, even when the overall moisture conditions along the swash zone are not conducive to high rates of evaporation. The formation of capillary barriers allows these moisture hotspots to persist over tidal cycles, leading to the retention of saltwater pockets within heterogeneous unsaturated finer sediments. As the swash zone recedes and evaporation intensifies, salt begins to accumulate near the beach surface. The moisture hotspots create preferential pathways that facilitate the penetration of hypersaline water into deeper, saturated sediments. In contrast, within the saturated zone, groundwater flow and salt transport are predominantly driven by preferential flow within high-permeability coarse sediments where capillarity is relatively low. Such transport and capillary mechanisms are crucial for a better understanding of coastal groundwater flow, interstitial habitats, biogeochemical conditions, and consequent nutrient cycling and contaminant transport in coastal zones. This highlights the necessity of considering integrated coastal physical drivers when investigating flow and transport processes in coastal swash zones.

1. Introduction

Coastal beaches are biogeochemically active systems, particularly the swash zone which hosts significant exchange of water and chemicals across the land-sea interface (Elfrink and Baldock, 2002; Geng et al., 2021a; Horn, 2006; Malott et al., 2016; Sous et al., 2016). This zone is characterized by high-frequency inundation and infiltration of seawater, driven by swash motion (Geng et al., 2017; Heiss et al., 2014; Sous et al., 2013). Consequently, salinity has been identified as a critical indicator in shaping the diversity and abundance of intertidal communities and their activities related to primary productivity and decomposition (Chambers et al., 2016; Lew et al., 2022). Elevated interstitial salinity has been linked to increased emergence rates for certain coastal species, such as platyhelminthes and copepods (Armonies, 1988; Zeppilli et al., 2018). In particular, hypersalinity can lead to cell dehydration, a decrease in turgor pressure, and impaired embryonic development

---

* Corresponding author at: Department of Earth Sciences, University of Hawai'i at Mānoa, Honolulu, HI 96822, USA.
E-mail address: xgeng@hawaii.edu (X. Geng).

https://doi.org/10.1016/j.jhydrol.2024.132322
Received 25 May 2024; Received in revised form 13 September 2024; Accepted 19 October 2024

(Einav et al., 2003; Nabavi et al., 2013; Şen, 2005). Additionally, studies have shown that hypersaline conditions limit the microbial degradation of oil residues deposited on Gulf beaches following the Deepwater Horizon oil spill (Abou Khalil et al., 2020; Geng et al., 2021b). Therefore, characterizing groundwater flow and salinity dynamics in the swash zone is crucial for understanding its role in regulating biogeochemical transformations and the associated biodiversity and abundance in coastal zones.

In coastal beaches, groundwater flow and salt transport processes are influenced by numerous physical driving factors. Among these, evaporation plays an important role in altering pore water flow pathways by increasing its salinity (Li et al., 2005; Silvestri et al., 2005; Zhang et al., 2014). In saline sediments, evaporation creates hydraulic gradients that drive upwelling pore water flow, leading to salt accumulation near the surface (Geng et al., 2016; Geng and Boufadel, 2015a). This accumulated salt reduces surface evaporation and establishes vertical density gradients, which in turn drive groundwater flow downwards. Research has shown that groundwater upwells in the swash zone due to evaporation near the sediment surface (Geng et al., 2023; Geng and Boufadel, 2015b; Zhang et al., 2014). These effects are more pronounced in coastal beach systems with relatively shallow groundwater tables (Geng and Boufadel, 2017; Xin et al., 2017). The rate of evaporation from the ground surface is influenced by the humidity gradient between the air and the land surface (Mahfouf and Noilhan, 1991). The high water content near the beach surface, facilitated by the shallow groundwater table, enhances the evaporation of pore water from the sediments. This shallow groundwater table also establishes a strong hydraulic connection between the evaporation front and deep groundwater, replenishing the water lost to evaporation from the surface and leading to a consistent evaporation rate (Liu et al., 2022).

Another critical factor influencing beach groundwater dynamics is the spatial heterogeneity of sediment permeability. Porous media are generally heterogeneous, which spatially and temporally alters groundwater flow and solute transport patterns, particularly in coastal regions (Adams and Gelhar, 1992; Dagan, 2012; Dentz et al., 2011; Gelhar, 1993; Geng et al., 2023, 2020a; Li et al., 2008a; Olorunsaye and Heiss, 2024; Sebben and Werner, 2016). Research has shown that spatial variability in sediment permeability can produce chaotic velocity fields that are similar to turbulent flow fields (Weeks and Sposito, 1998). Beach heterogeneity has been identified in prior studies (Gallagher et al., 2016; Neal et al., 2002). Despite extensive modeling efforts to investigate coastal groundwater and salinity dynamics, studies often focus on the impact of a single driving factor (Geng et al., 2014; Heiss et al., 2017; Li et al., 2008b; Lu et al., 2013; Robinson et al., 2014; Wilson and Gardner, 2006; Xin et al., 2010), such as tides, waves, evaporation, and heterogeneity, or the combined impacts of two of the aforementioned factors (Geng et al., 2023, 2020b, 2020a; Geng and Boufadel, 2015c; Heiss et al., 2020; Wang et al., 2023; Xin et al., 2017; Zhang et al., 2021). Currently, no comprehensive field measurements or numerical simulation exist that incorporate aerodynamics, high-frequency seawater inundation, and subsurface flow dynamics to explore the integrated role of multiple driving factors and complex geology in regulating swash zone dynamics.

Groundwater and salinity dynamics in the swash zone are influenced by individual waves. As waves approach the shore and encounter shallower water depths, they become unstable and break. The resulting bore leads to complex pressure oscillations along the swash zone surface, generating significant interaction and exchange between seawater and groundwater. Phase-resolving modeling of surface waves, which explicitly reproduces the sea surface and velocity field evolution using turbulence models, is computationally expensive (Bakhtyar et al., 2011; Geng et al., 2014; Hirt and Nichols, 1981; Wilcox, 1998, 1993). To more effectively simulate wave effects on swash groundwater dynamics, simplified approaches have been developed, though they often neglect the high-frequency response of subsurface flow and moisture content to individual waves (Geng and Boufadel, 2015c; Robinson et al., 2014; Xin et al., 2010). Site-specific modeling has also been conducted, where high-frequency wave-induced pressure oscillations along the beach surface were measured and adopted for groundwater simulations (Geng et al., 2020b, 2017).

The objective of this paper is to evaluate the effects of heterogeneous hydraulic conductivity and capillarity on groundwater flow and salinity dynamics in the swash zone, subjected to temporally alternating effects of wave swash and evaporation (Fig. 1). Specifically, the numerical study presented herein is based on a field study conducted on a beach with wave swash (Heiss et al., 2015). Geologic heterogeneity was modeled using permeability datasets collected from the Upper Cretaceous Straight Cliffs Formation near Escalanete, Utah, which represents a wide range of fluvial to marine depositional settings, including both wave-dominated and tide-dominated nearshore-marine environments (Castle et al., 2004). Simulations of subsurface flow and salt transport were conducted through a 2-D density-dependent variably saturated model within a Monte Carlo framework. For comparison, an additional simulation was performed with a homogeneous K field that had the same geometric mean as the heterogeneous sediments (2.4×10^{-4} m/s). Tempo-spatial patterns of swash zone pore-water flow and salinity were quantified for a deep understanding of the controls of geologic heterogeneity on flow and mixing dynamics in the swash zone of beach aquifers.

2. Methodology

2.1. Field measurements from prior work

Field measurements of pore pressure, moisture content, and runup location were conducted on a beach located at Herring Point, Cape Henlopen, DE, USA (Figure S1). At this site, a cross-shore transect of six instrument arrays of moisture sensors (Meter Environmental EC-5 Soil Moisture Sensors) was installed in the upper beachface. The position of the instrument transect was chosen such that the transect spanned the swash zone at high tide. The moisture sensors were fixed at 4–6-cm depth intervals on each vertical array, beginning at 2 cm depth and reaching a maximum depth of 24 cm. These moisture sensors were used to characterize saturation fluctuations in response to swash motions. Pressure transducers (Druck PTX 1835) were mounted at the bottom of each instrument array to capture the effects of tide and swash forcing on pore pressure oscillations and thus groundwater table fluctuations.

Pressure transducers were also affixed to four of the arrays at the sand surface. These surface pressure transducers recorded surface water pressure variations, allowing us to determine when the transect was inundated by swash. Saturation and pore pressure were recorded at 5 and 16 Hz, respectively. Tides were semidiurnal with a mean tidal range of 1.4 m. As a result, the studied transect was exposed to wave swash for approximately 8 h within a tidal cycle. Further details regarding the field measurements can be found in Heiss et al. (2015).

2.2. Representation of heterogeneous fields

Geophysical fields (e.g., hydraulic conductivity K field) have been widely observed to be self-similar or so-called scaling invariant (Boufadel et al., 2000; Peitgen and Saupe, 1988). Scaling properties of a K field at the support scale h can be characterized using the sth order structure function:

$$\langle \lceil \Delta K_h \rceil^s \rangle \; h^{-\xi(s)} \tag{1}$$

where the function $\xi(s)$ is the structure function exponent. In this study, heterogeneous K fields were assumed to follow multifractal scaling, which captures both Gaussian and non-Gaussian statistics.

Heterogeneous K fields were generated based on permeability data measured from a portion of the Upper Cretaceous Straight Cliffs Formation near Escalanete, Utah (Castle et al., 2004). This dataset

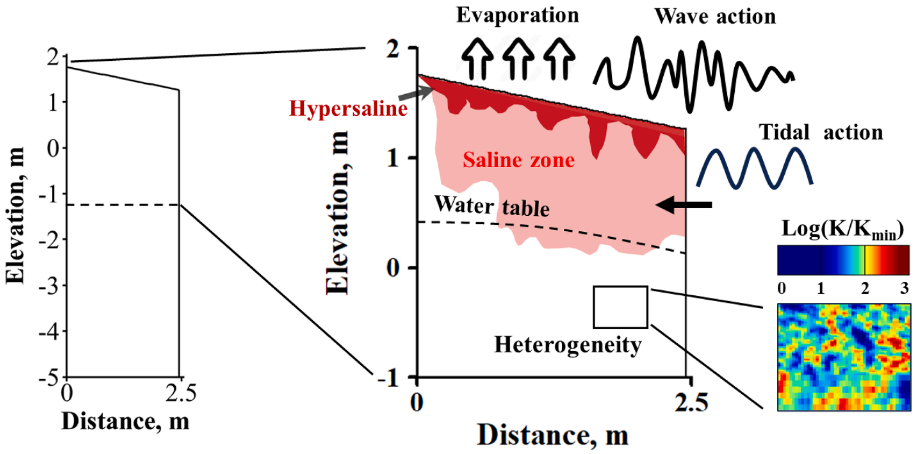

Fig. 1. Conceptual model of salinization process in swash zone influenced by tides, waves, evaporation, and geologic heterogeneity. Groundwater flow and salt transport simulations were conducted using field data collected from a sandy beach at Herring Point, Cape Henlopen, DE, USA (Figure S1). Sediment heterogeneity was modeled based on permeability data from the Upper Cretaceous Straight Cliffs Formation near Escalanete, Utah, which represents a wide range of fluvial to marine depositional settings, including both wave-dominated and tide-dominated nearshore-marine sediment environments.

comprises approximately 500 permeability measurements taken at a sample spacing of 15 cm along four vertical transects and three horizontal transects, representing a wide range of fluvial to marine depositional settings, including both wave-dominated and tide-dominated nearshore-marine environments. In our previous study (Geng et al., 2020c), the permeability data from the Utah sites exhibited multifractal isotropic scaling, as evidenced by the nearly linear relationship between the power spectral density and spatial lag on a log–log plot (Figure S2). Consequently, heterogeneous K fields were generated using the Universal Multifractal model, with the multifractal properties derived from the Utah data as input. In the UM model, the function $\xi(s)$ is expressed as follows (Pecknold et al., 1993; Schertzer and Lovejoy, 1987):

$$\xi = sH - \frac{C1}{\alpha' - 1}\left(s^{\alpha'} - s\right) \tag{2}$$

where α' $(0 < \alpha' \leq 2)$ is the multifractal parameter, measuring departure from monofractal behavior defined by $\alpha' = 0$; $c1$ is the codimension parameter, measuring the degree of intermittency; and H is the Hurst exponent linked to the degree of scale-invariant smoothing. To mitigate any potential bias originating from the boundaries, the 2D fractal K field was generated over 512 × 512 cells at 5 cm × 5c m resolution, and the central 140 × 50 cells were extracted and used for groundwater flow and transport modeling. Thirty realizations were generated with the geometric mean of 2.4×10^{-4} m/s and the standard deviation of 4.4×10^{-4} m/s. The generated multifractal fields were tested to preserve the same underlying statistics as the measurement fields by comparing observed and simulated structure function exponents (i.e., ξ). The details of generating multifractal K fields are described in Geng et al. (2020c). A homogeneous case with the equivalent K to the heterogeneous case was simulated for comparison. Following von Jeetze et al. (2020), parameter α was used to reflect spatial heterogeneity of capillarity properties and a linear correlation was assumed between α and K

$$\frac{K_1}{K_0} = (1 + 0.1R_N)\frac{\alpha_1}{\alpha_0} \tag{3}$$

where K_i and α_i, where $i = 0, 1$, represent the hydraulic conductivity and the van Genuchten parameter which represents an estimate of the thickness of the capillary fringe, for two different sediment types, respectively, and R_N is a uniformly distributed random variable between 0 and 1, accounting for certain perturbation of the correlation.

2.3. *Groundwater flow and solute transport model*

Subsurface flow and solute transport were simulated using the variably saturated density-dependent model MARUN (Boufadel et al., 1999; Geng et al., 2017; Geng and Boufadel, 2015b). The simulated domain represented a 2-D cross-section of a beach aquifer, measuring 2.5 m in length and approximately 6 m in depth (Fig. 1), extending horizontally from the landward to seaward instrument arrays. The mesh resolution was approximately 5 cm in the horizontal direction and about 2 cm above and 5 cm below elevation $z = 0$ in the vertical direction. Pressure data measured by the transducers at the beach surface were interpolated across the transect and assigned to each surface node to represent swash forcing. A freshwater salinity of 0.0 g/L was assigned at the landward boundary. The model performed a check on the surface nodes: a Dirichlet boundary condition of 35.0 g/L was assigned for the nodes where seawater infiltrated, and a Cauchy boundary condition was assigned to the nodes exposed to the air to simulate evaporation-induced salt accumulation. The time step was automatically adjusted by the model to ensure convergence criteria were met (Courant number < 1). This site-specific numerical model has undergone extensive validation in our earlier research on groundwater dynamics in the swash zone (Geng et al., 2020b, 2017), where evaporation effects were not taken into account. The parameter values used for the simulations are reported in Table 1.

2.4. *Evaporation*

Evaporation occurred on the portion of the surface exposed to the air. A Neumann boundary condition was adopted on the surface to simulate evaporated water flow, and the evaporation flux, E_g, was calculated using the bulk aerodynamic approach (Mahfouf and Noilhan, 1991):

$$E_g = \frac{\rho_{air}}{\rho_{water}R_{air}}\left(q_g - q_{air}\right) \tag{4}$$

Here, ρ_{air} and ρ_{water} represent the density of air and freshwater, respectively, q_a and q_g are the air and surface relative humidity, and R_{air} is the aerodynamic resistance, expressed as $94.909 \times u^{-0.9036}$, where u represents the wind speed at the atmospheric reference level (~2 m above the sand surface). A Cauchy boundary condition was adopted in the MARUN model to simulate solute accumulation below the soil surface due to evaporation, expressed as follows (Geng and Boufadel, 2015b):

$$\left(\vec{q}c - \beta\phi SD\cdot\nabla c\right)\cdot\vec{n} = 0 \tag{5}$$

Here $\overrightarrow{q}$ is the Darcy flux vector, c is the solute concentration, β is the density ratio between actual water density to freshwater density, ϕ is the porosity of the porous medium, S is the soil moisture, D represents the physical dispersion tensor, $\overrightarrow{n}$ is the vector normal to the boundary. In this study, we established meteorological parameters of 20 % relative humidity during the day and 80 % at night, a temperature of 27 °C, and a wind speed of 8.94 m/s to represent the typical dry summer climate observed in Lewes, Delaware. The potential evaporation rates were estimated to be 1.6×10^{-6} m/s during the day and 3.9×10^{-7} m/s at night. Numerical simulations were initially conducted without evaporation. After the system reached a quasi-steady state, evaporation was introduced into the model. The simulations were continued over multiple tidal cycles until a quasi-steady state was achieved. The results presented in the paper, spanning a two-day period, reflects this quasi-steady state, where evaporation-induced salinity increases are eventually diluted and washed out by subsequent swash motion before the next cycle of evaporation begins.

3. Results

3.1. Effects of heterogeneity on variably saturated hydraulic conductivity

Sediment heterogeneity creates spatial variability in hydraulic conductivity, due to differences in both the permeability and capillary properties in variably saturated beaches (Fig. 2). Hydraulic conductivity, denoted as K, is calculated as $k_r K_0$, where the relative permeability k_r varies between 0 and 1, representing variably saturated conditions, and is equal to 1 when porous media are fully saturated, and K_0 represents saturated hydraulic conductivity (Equation (3). As shown in Fig. 2a and 2b, for each simulated model cell, a higher K results in a lower theoretical capillary fringe ($1/\alpha$) height, due to the linear relation between K and the van Genuchten parameter α. The selected K values at the 5th, 25th, 50th, 75th, and 95th percentiles from the heterogeneous fields illustrates the combined effects of heterogeneous permeability (i.e., saturated hydraulic conductivity) and heterogeneous capillarity (i.e., α) on actual hydraulic conductivity (Fig. 2c). When the sediment is fully saturated, hydraulic conductivity depends solely on its saturated values. As the sediment pores begin to drain, the sediments become unsaturated, indicated by the pore pressure decrease from zero (i.e., saturated) to negative (i.e., unsaturated). Hydraulic conductivity decreases rapidly and signficantly for high percentiles of K (i.e., high K values). In contrast, for low percentiles of K (i.e., low K values), the hydraulic conductivities maintain their saturated levels across a wider pressure range before gradually decreasing as the pore pressure continues to drop (Fig. 2c). Notably, sediment at the 5th percentile K maintains its saturated level at pressures as low as −0.6 m, compared to sediment at the 95th percentile K, which begins to decrease when the pressure drops below just −0.05 m.

3.2. Evaporation and salinity dynamics in the swash zone

Waves dynamically alter the evaporation rate, subsequently affecting the near-surface salinity in the swash zone of both homogeneous and heterogeneous sediments. As demonstrated in Fig. 3a and 3b, high-frequency wave motion in the swash zone causes significant fluctuations in evaporation rates. During periods of wave run-up, the top of the model domain is inundated, temporarily halting evaporation and increasing water content within the near-surface sediments. Conversely, during wave run-down, the exposed high-moisture sediments promote evaporation at the swash zone's surface. As the swash zone waves recede seaward during falling tide, there is a gradual decrease in evaporation rate over time (e.g., between time t = 12 h and 17 h), correlating with a decline in surface moisture as shown in Fig. 3c. The evaporation rate is slightly higher in the heterogeneous case due to its relatively greater overall moisture content near the beach surface, which is attributed to the presence of smaller grained material that holds moisture. Notably, there is an apparent inconsistency between the increase in evaporation rates and the salinity at the swash zone surface. During periods of significant fluctuations in the evaporation rate, specifically between times t = 3h and 10 h, the near-surface salinity in the homogeneous case does not exceed that of seawater (Fig. 3d). This is likely due to the rapid dilution of accumulated salt by seawater infiltration when frequent swash events inundate the surface of the model domain. In contrast, in the heterogeneous case, the near-surface salinity is slightly elevated above the seawater level during this period, likely due to the higher evaporation rate compared to the homogeneous case. In contrast, during periods when waves recede seaward during falling tide, the average salinity within the top 5 cm of sediment significantly increases from seawater levels (35 g/L) to nearly 90 g/L and 70 g/L, for heterogeneous and homogeneous cases, respectively, indicating substantial salt accumulation even as the evaporation rates gradually drop. The higher peak salinity in the heterogeneous case is due to a higher overall evaporation rate at the beach surface. The temporal evolution of the areal extent of evaporation-induced high salinity (> 35 g/L of seawater salinity) and hypersaline (>45 g/L, defined as a threshold of hypersalinity) zones also reflects these distinct patterns: the spatial extent of the hypersaline plume increases with the absence of swash inundation due to evaporation and is rapidly diminished by subsequent swash action (Fig. 3e-3f). These results highlight the complex interplay between waves and evaporation on altering near-surface salinity along the swash zone.

The combined effects of wave swash and geologic heterogeneity significantly influence the temporal and spatial trends in evaporation along the swash zone. Our simulation results show high-frequency

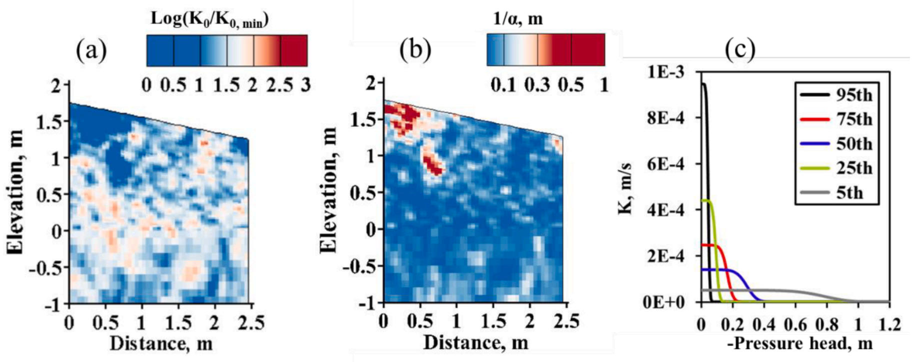

Fig. 2. Example distributions of (a) saturated hydraulic conductivity (K0) and (b) height of capillarity fringe as the porous medium becomes unsaturated (1/α) from one of 30 geologic heterogeneous realizations. (c) Example K at different percentiles—5th, 25th, 50th, 75th, and 95th—as a function of pressure potential, where a pressure of zero indicates saturated conditions, while negative pressure indicates unsaturated conditions.

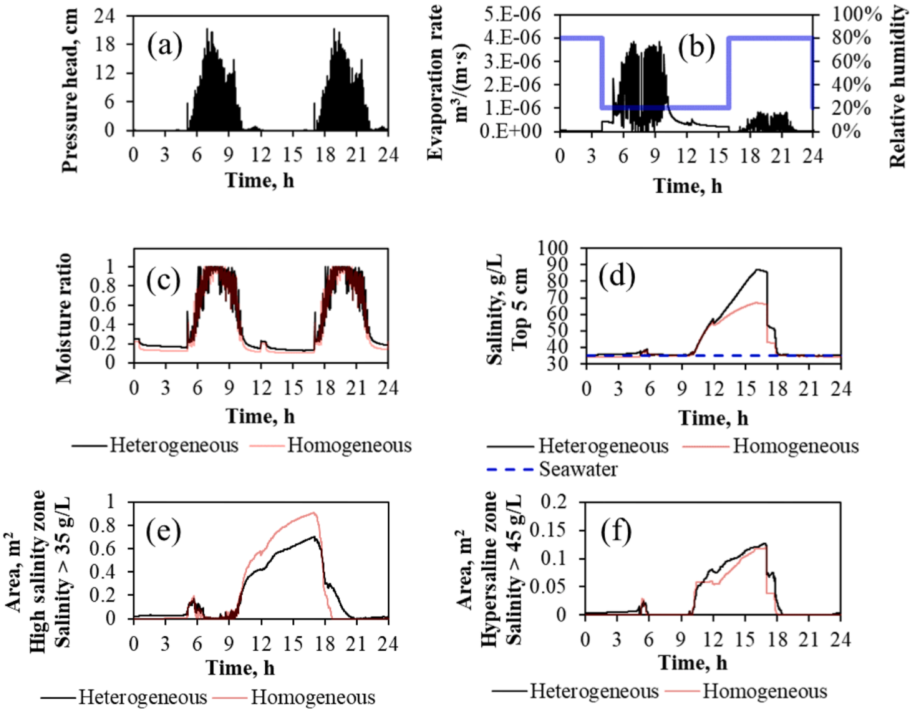

Fig. 3. Temporal evolution of (a) swash-induced pressure oscillation measured at the beach surface using the pressure transducer deployed at x = 2.08 m; (b-c) simulated average evaporation rate and moisture ratio along the swash zone; (d) simulated average salinity within the top 5 cm of the sediment in the swash zone; and (e) the simulated areal extent of evaporation-induced high salinity and hypersaline zones, where salinity exceeds 36 g/L (seawater) and 45 g/L, respectively, illustrated for the homogeneous case and a representative heterogeneous case.

variations in the spatial extent of the evaporation rate along the beach surface (Fig. 4a). These variations correlate strongly with the temporal fluctuations in the overall evaporation rate in this zone. This suggests that the overall intensity of evaporation along the simulated beach domain is largely governed by its changing spatial extent which is influenced by waves. However, as the waves recede seaward during falling tide, geologic heterogeneity exerts a strong control over the spatial patterns of evaporation (Fig. 4b-4i). The results indicate that the spatial extent of evaporation is lower in the heterogeneous case than in the homogeneous case when waves recede seawater during falling tide (e.g., between time t = 12 h and 17 h in Fig. 4a). This is due to areas of low capillarity (high K aggregates) on the heterogeneous sediment surface that retain insufficient moisture to trigger evaporation (e.g., between $x = 0.5$ m and $x = 0.7$ m in Fig. 4b-4e). When the swash zone moves seaward of the model domain during falling tide, evaporation rates and moisture content in the homogeneous case show a spatially uniform distribution across the evaporation surface (Fig. 4f-4i). This spatial uniformity is attributed to the homogeneity of the sediments, which drain water almost evenly, maintaining a stable humidity gradient conducive to evaporation. In contrast, in the heterogeneous case, evaporation rates exhibit significant spatial variation both when the model domain is inundated by swash and when it is not (Fig. 4 column 1, black lines). This spatial variaiblity of evaporation rate mirrors the spatial distribution of moisture (Fig. 4 column 2, black lines). The heterogeneous capillary properties of the sediments spatially control the capacity of local-scale sediments to retain moisture as they become unsaturated, thus causing varying evaporation rates. Specifically, high capillary zones (low K aggregates) retain moisture that consistently support high evaporation rates at the surface (e.g., between $x = 0.7$ m and $x = 1.0$ m in Fig. 4b-i), whereas, low capillary zones promote groundwater drainage, leading to relatively low moisture levels that impede surface evaporation (e.g., between $x = 0.5$ m and $x = 0.7$ m).

Geological heterogeneity strongly influences pore water salinity in the swash zone through its control on the average evaporation rate. Fig. 5a shows the average evaporation rate over two tidal cycles (i.e., 24 h), and Fig. 5b shows salinity averaged within the top 5 cm of sediment between times t = 10*h* and 18 h, which is when salt accumulation occurs. In the homogeneous case, a nearly spatially uniform evaporation rate forms along the simulated beach surface. Similarly, the salinity distribution is to some extent uniform, remaining at 60 g/L, except for a lower salinity at the most landward side due to fresh groundwater recharge, and a relatively higher salinity at the seaward side due to slightly higher evaporation rates. In contrast, in the heterogeneous cases, both the averaged evaporation rate and the resulting salinity exhibit significant spatial variation across the beach surface. Although the average evaporation rates are comparable between the homogeneous and heterogeneous cases, the evaporation rates among the heterogeneous cases show large variations. The maximum evaporation rate and salinity reach about 4.5×10^{-8} $m^3/(m\cdot s)$ and 140 g/L, respectively, which are over four times and two times higher than their averages. These results indicate that local-scale heterogeneity, particularly the presence for high capillarity zones near the surface leading to high air-entry pressure, significantly increases the spatial variability of hypersalinity that form near the sand surface due to evaporation.

3.3. Subsurface development of evaporation-induced high salinity plume

The interaction between wave swash, evaporation, and heterogeneity drives a complex spatial evolution of a saline plume beneath the swash zone. The simulation results demonstrate the following dynamics: During periods when waves recede seaward during falling tide, evaporation leads to increased salt accumulation, resulting in the formation of a high salinity plume near the swash zone surface that is denser than seawater (Fig. 6). This high salinity plume notably expands at the lower portion of the model domain (e.g., time t = 10.5 h and 16.5 h). When waves begin impacting the top of the domain, the high-salinity plume is pushed landward and downward due to wave-induced seawater infiltration, becoming diluted by the surrounding low-salinity groundwater (e.g., time t = 17.5 h). During periods of intense wave activity on the

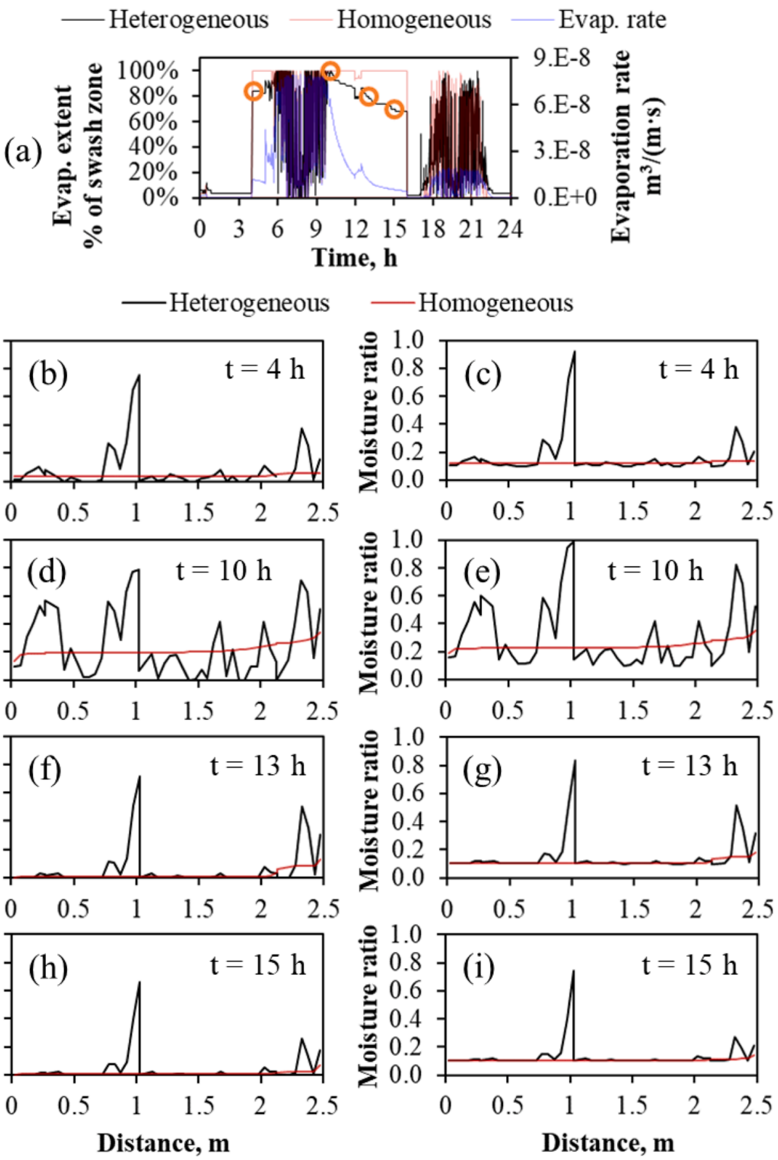

Fig. 4. (a) Temporal evolution of evaporation spatial extent (% of swash zone). (b-i) Spatial distribution of evaporation rate (left panel) and moisture ratio (right panel) along the swash zone surface at times t = 4h, 10 h, 13 h, and 15 h, respectively, marked as orange circles in Fig. 4a. (For interpretation of the references to colour in this figure legend, the reader is referred to the web version of this article.)

swash zone, such as at times t = 18 h and 19 h, the high-salinity plume near the seaward portion diminishes due to progressive dilution by swash infiltration. Consequently, the high-salinity plume forms only under the landward portion of the simulated sand surface, where the effects of the swash are minimal. This dynamic interaction leads to spatial variation in salinity along the swash zone over time. The impacts of geologic heterogeneity on the spatial evolution of the evaporation-induced high-salinity plume are also apparent. Compared to the homogeneous case, salt fingers form near the beach surface when evaporation starts to elevate the near-surface salinity (e.g., at time t = 10.5 h). These dense salt fingers further develop at time t = 16.5 h, creating high-salinity hotspots at the surface. The results indicate that local heterogeneity coupled with evaporation creates a more unstable flow field under the swash zone compared to homogeneous sediments.

Wave motion leads to dynamic changes in moisture conditions within the swash zone (Fig. 7), which strongly affect its salinity evolution (Fig. 6). In the homogeneous case, the moisture ratio is relatively higher near the lower part of the simulated domain due to more frequent inundation by wave-induced seawater infiltration as well as shallower groundwater table (e.g., the upper panel in Fig. 7 at time t = 10.5 h). This elevated moisture accounts for the higher salinity levels observed in this area (e.g., the upper panel in Fig. 6 at time t = 16.5 h). As waves approach the simulated domain, seawater infiltration at the wavefronts increases the moisture ratio (e.g., the upper panel in Fig. 7 at times t = 17.5 h, 18 h, and 19 h), diluting the accumulated salt at these locations (e.g., the upper panel in Fig. 6 at times t = 17.5 h, 18 h, and 19 h). As a result, the evaporation-induced high-salinity zone tends to move further landward due to swash motion. The simulation results highlight the critical role of water content in modulating pore-water salinity along the swash zone through evaporation. When evaporation occurs, the relatively high moisture near the surface of the swash zone creates a pronounced humidity gradient, leading to a high evaporation rate and consequently, an intense accumulation of salt near the surface. Conversely, as waves approach the simulated domain, the increased moisture aids in diluting the hypersaline concentrations back to the level of seawater salinity (e.g., the upper panel in Fig. 6 at times t = 17.5 h, 18 h, and 19 h). Our simulation results show that following wave-induced seawater infiltration, heterogeneous capillarity creates capillary

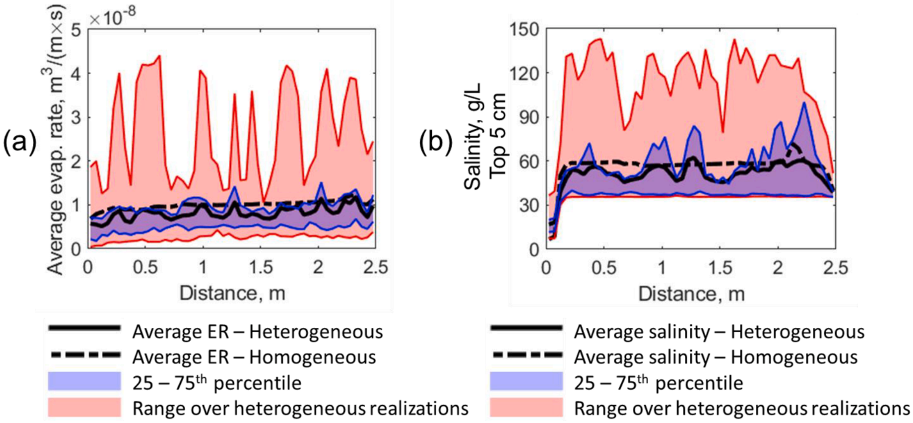

Fig. 5. Spatial distribution of (a) the evaporation rate, averaged over a tidal cycle (i.e., 24 h), and (b) salinity, averaged within the top 5 cm of the sediment and over 8 h between time t = 8h and 18 h when apparent salt accumulation occurs. The ranges between the 25th and 75th percentiles, and between the minimum and maximum, are also shown as blue and red shades, respectively, accounting for all the heterogeneous cases. (For interpretation of the references to colour in this figure legend, the reader is referred to the web version of this article.)

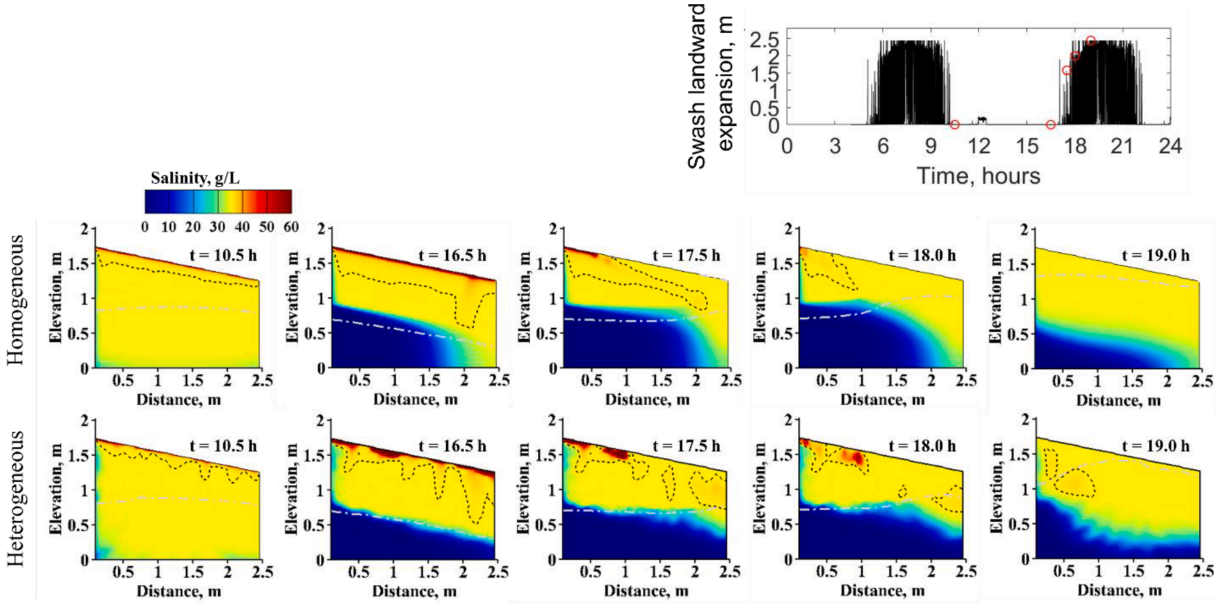

Fig. 6. Simulated salinity at different times within a tidal cycle for both homogeneous (upper panel) and heterogeneous (lower panel) cases. The dotted contours represent the edge of evaporation-induced high-salinity plume (salinity > 35 g/L). The results for the heterogeneous case correspond to the heterogeneous field illustrated in Fig. 1. Swash landward expansion along the simulated domain is provided in the rightmost panel where the time points selected for salinity contours are marked as circle symbols.

barriers, where capillarity tension prevents groundwater flow from the low-permeability units to the surrounding high-permeability units. This leads to the retention of saltwater within high capillarity (low-K) zones, thereby creating moisture hotspots within the unsaturated zone. The hydraulic conductivity at these moisture hotpots within unsaturated zone is relatively higher than in the surrounding areas, which has strong implications for the spatial evolution of the evaporation-induced high-salinity plume in the subsurface.

Capillarity is an important control on preferential flow in the unsaturated zone of swash zones with geologic heterogeneity, while permeability is the primary controlling factor for saturated groundwater flow. These contrasting effects significantly influence the evolution and pathways of the evaporation-induced high-salinity plume in the subsurface. In the homogeneous case, as the tide and swash zone recede seaward of the simulated beach domain, percolating seawater continues to flow vertically through the unsaturated zone to the water table, where it then flows seaward driven by the large-scale terrestrial hydraulic gradient (Fig. 8a-8b). As waves approach the simulated sand surface, seawater starts to saturate the surface sediments. This forms a wedge of high moisture content near the beach surface that rapidly expands both landwards and downwards as the swash zone moves further inland (Fig. 8c-8d). Swash-induced seawater infiltration forms a water table mound, resulting in seaward flow on the sea side of the mound and landward flow on the land side (Fig. 8c-8d). Similar flow patterns are observed in the heterogeneous case; however, velocity magnitudes are highly irregular across space due to the heterogeneous permeability and capillarity (Fig. 8e-8 h). Notably, localized areas of high pore-water velocities extend from the sand surface, through the unsaturated zone, and into the saturated zone, creating dendritic preferential flow paths in the sediments with higher hydraulic conductivity. The spatial expansion of the high-salinity plume in the heterogeneous case tracks the beginning of the preferential flow pathways in the unsaturated zone (Fig. 8i-8 l). Within the unsaturated zone in heterogeneous media, areas of high capillarity retain a high moisture content. Consequently, the

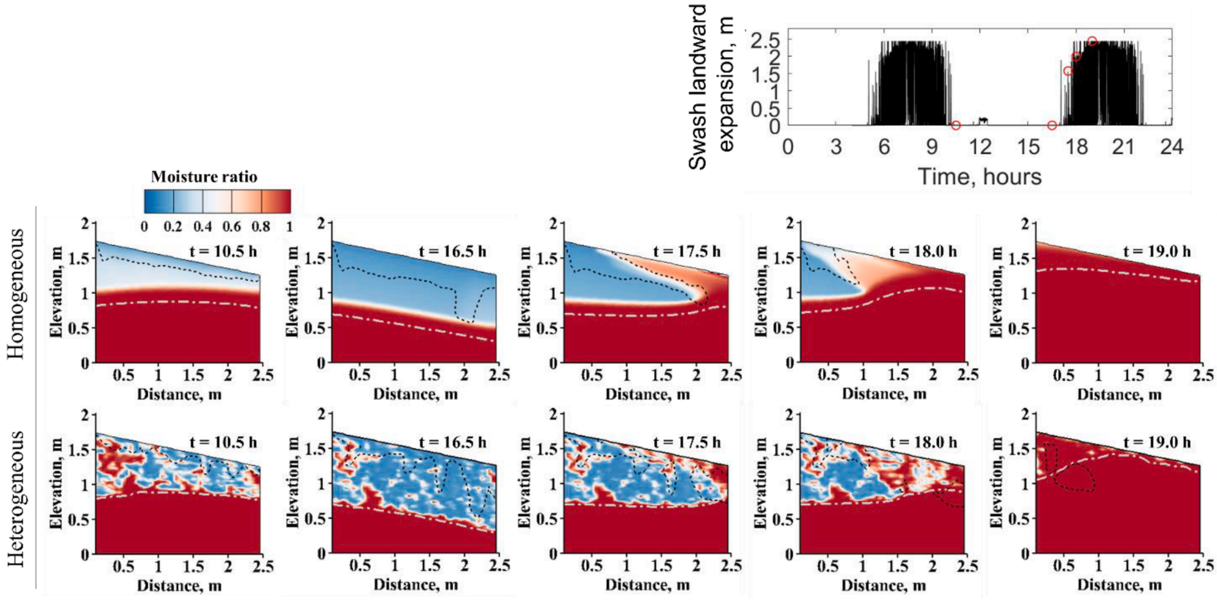

Fig. 7. Simulated moisture ratio at different times within a tidal cycle for both homogeneous (upper panel) and heterogeneous (lower panel) cases. The dotted contours represent the edge of evaporation-induced high-salinity plume (salinity > 35 g/L). The results for the heterogeneous case correspond to the heterogeneous field illustrated in Fig. 1. Swash landward expansion along the simulated domain is provided in the rightmost panel where the time points selected for moisture contours are marked as circle symbols.

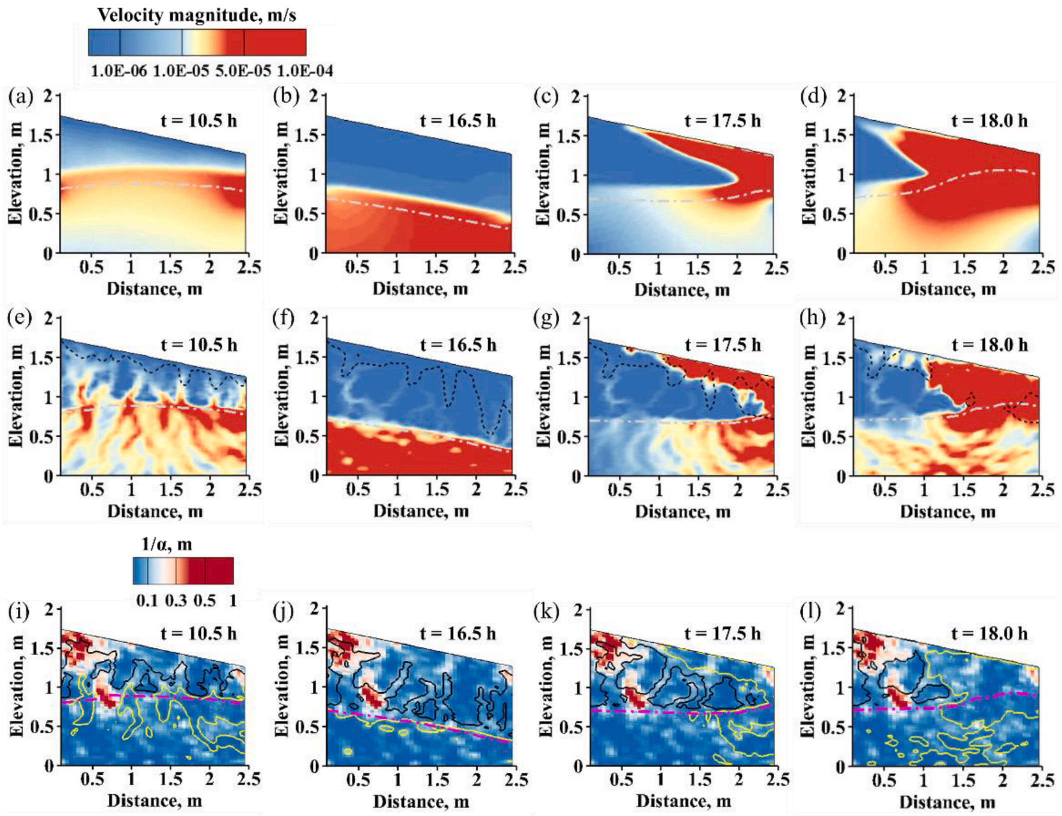

Fig. 8. Simulated flow velocities within the swash zone for (a-d) homogeneous and (e-h) heterogeneous cases at different times within a tidal cycle. The gray contour in panels a-h represents the water table. The dotted contour represents the edge of evaporation-induced high-salinity plume (salinity > 35 g/L). Panels (i-l) show the spatial distribution of the theoretical height of the capillarity fringe, calculated using Eq. (3). The black and yellow contours in panels i-l delineate zones where preferential flow occurs within unsaturated and saturated zones, respectively. The black contours are velocities of 5 × 10–6 m/s in Fig. 8i and 5 × 10–7 m/s in Fig. 8j-8 l, while yellow contours are velocities of 3 × 10–5 m/s. The results for the heterogeneous case correspond to the heterogeneous field illustrated in Fig. 1. (For interpretation of the references to colour in this figure legend, the reader is referred to the web version of this article.)

evaporation-induced high salinity plume predominately evolves along connected high capillary zones, penetrating downward into deeper saturated zones (black dotted contours shown in Fig. 8e-8 h). In contrast, within the saturated zone, preferential groundwater flow pathways emerge through zones with high permeability, where capillarity is relatively low.

Waves and evaporation recursively impact the depth of the hypersaline plume beneath the swash zone. In Fig. 9a-9b, the penetration depth of the hypersaline plume (salinity > 45 g/L) varies with the periodic motion of waves in the swash zone, reaching its maximum depth during periods when waves recede during falling tide. On average, the plume extends to a depth of ∼ 3 cm in both heterogeneous and homogeneous cases. However, the maximum penetration depth for the heterogeneous case is much greater, reaching as deep as 30 cm, compared to the maximum penetration depth of 6 cm for the homogeneous case. This is due to the formation of preferential flow pathways from heterogeneous capillarity, which allow the hypersaline plume to penetrate deeper into the subsurface. Consequently, the resulting salt fingers significantly increase the downward flux of salt. Additionally, the hypersaline plume persists for a longer period in the heterogeneous case than in the homogeneous case (Fig. 9a). This is likely because localized moisture hotspots, generated within high capillarity zones, can still support evaporation, even when the overall moisture conditions near the sand surface are not conducive to evaporation. This allows the hypersaline plume to emerge earlier and last for an extended period. The vertical salinity profiles, shown in Fig. 9b-9c, reveal a significant decrease in salinity with increasing depth for both the homogeneous and heterogeneous cases. Notably, at times t = 10*h*, 12h, and 16 h, the horizontally averaged salinity nearly reaches 150 g/L and 120 g/L in the heterogeneous and homogeneous cases, respectively, but then decreases to below 40 g/L within a 20 cm depth. This pattern indicates that although salinity is extremely high near the sand surface, the accumulated mass of salt is relatively low compared to the volume of surrounding saline water. This difference allows for rapid dilution, effectively preventing the formation of a persistent hypersaline plume in the deep sediments beneath the swash zone.

Descriptive statistics show that the maximum penetration depth of the evaporation-induced high-salinity plume is consistently higher for the heterogeneous cases compared to the homogeneous case (Fig. 10a and 10b). The maximum penetration depth of the high-salinity plume (salinity > 35 g/L) for the homogeneous case is within 100 cm; in contrast, the maximum depth of the plume within the heterogeneous sediments can be as deep as 200 cm beneath the beach surface. Furthermore, the maximum penetration depth in the heterogeneous models shows significant spatial variation. This is due to heterogeneous capillarity and permeability, which create vertical preferential flow and transport paths in the unsaturated and saturated zones, as discussed previously. In contrast, the hypersaline plume (salinity > 45 g/L) develops within just ∼ 5 cm of the sand surface for the homogeneous case, and as deep as 40 cm in heterogeneous cases. The vertical profiles in Fig. 10c show that within heterogeneous sediments, the evaporation-induced high salinity plume not only extends deeper, but also exhibits higher maximum salinity (Fig. 10c). The average maximum salinity is higher at all depths for the heterogeneous cases. The penetration depth as well as the maximum salinity for the homogeneous case are comparable to the minimum values of the heterogeneous cases. This indicates that geologic heterogeneity facilitates spatial evolution of the evaporation-induced high-salinity plume in the subsurface, increasing both its spatial expansion as well as salinity levels. Descriptive statistics also indicate that sediment heterogeneity leads to signficiant variation in moisture content along the swash zone surface (Fig. 10d). The resulting moisture hotspots intensify evaporation and promote the vertical penentration of evaporation-induced hypersaline plumes.

4. Discussion

Our study highlights the dynamic changes in moisture and salinity within the swash zone, governed by the combined effects of wave action, evaporation, and geologic heterogeneity. In particular, under certain sediment properties and atmospheric conditions, evaporation triggers a hypersalinity zone at the surface of the swash zone, which then migrates downwards due to vertical density and hydraulic gradients. Heterogeneity creates moisture hotspots and induces unstable development of a hypersaline plume beneath the swash zone, following preferential groundwater flow pathways. Such transport mechanisms can strongly affect the biogeochemical conditions beneath swash zones. For example, in marine sediments, moisture content significantly impacts the habitat of microbial communities and associated biogeochemical processes such as nitrogen mineralization and nitrification (Cassman and Munns, 1980; Guntiñas et al., 2012). The salinity of pore water is also crucial for the functioning and ecological services of beach environments (Chambers et al., 2016; Jia et al., 2019; Lew et al., 2022). Previous research reveals that hypersalinity hampers the microbially mediated uptake of dissolved organic carbon (DOC) and dissolved organic nitrogen (DON) (Paerl and Yannarell, 2010; Yannarell and Paerl, 2007). This occurs because increased salinity leads to cell dehydration and a reduction in turgor pressure, which are essential for maitaining cell structure and function (Nabavi et al., 2013; Oren, 2008). Additionally, the high ionic strength

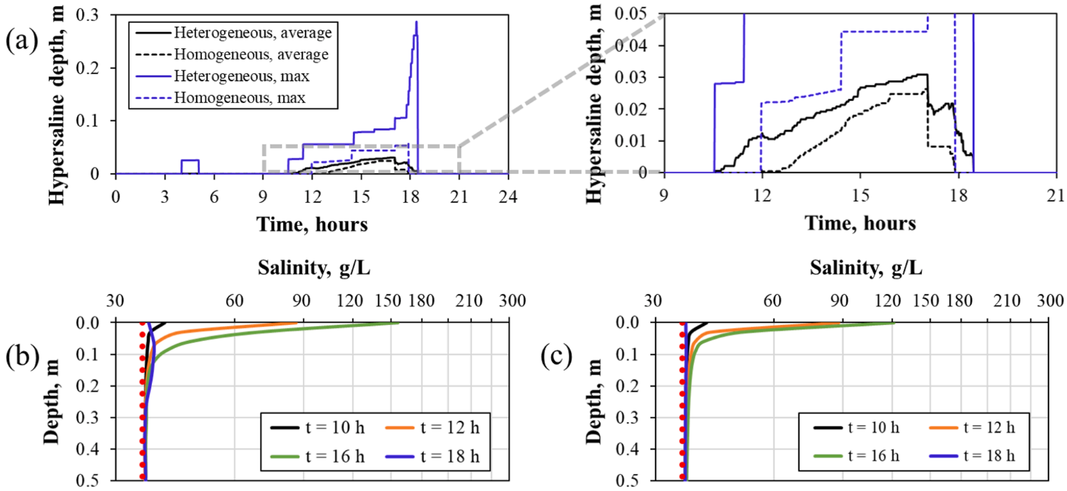

Fig. 9. (a) Temporal evolution of hypersaline depth in the swash zone for heterogeneous and homogeneous cases. (b-c) Vertical distribution of salinity, representing the horizontal average at each depth, at times t = 10 h, 12 h, 16 h, and 18 h, for heterogeneous (left) and homogeneous cases (right).

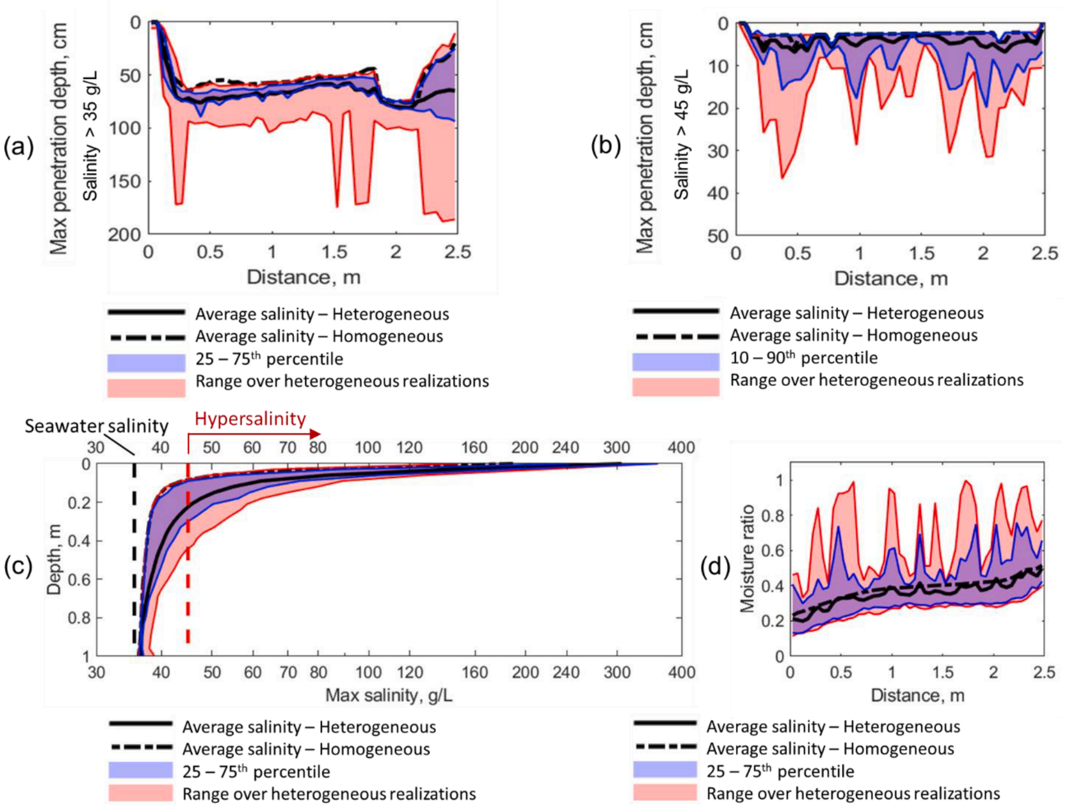

Fig. 10. Spatial distribution of the averaged maximum penetration depth for evaporation-induced (a) high salinity plumes where salinity exceeds that of seawater (35 g/L) and (b) hypersaline plumes where salinity exceeds 45 g/L. Panel (c) shows the vertical distribution of maximum salinity, representing the horizontal average at each depth. The percentile ranges, and the minimum and maximum values, are shown in blue and red shades, respectively, accounting for all the heterogeneous cases. Panel (d) shows the spatial distribution of the averaged moisture ratio along the swash zone surface. (For interpretation of the references to colour in this figure legend, the reader is referred to the web version of this article.)

in hypersaline environments can interfere with microbial communication and biofilm formation, further reducing microbial activity (Grattieri and Minteer, 2018). Thus, our model results of the combined effects of evaporation and geologic heterogeneity on temporal and spatial dynamics of moisture content and salinity in the swash zone is likely to have profound implications for biogeochemical processes in coastal beach environments.

Our study highlights the importance of geologic heterogeneity in the transport dynamics of the swash zone. In coastal marine systems, the supralittoral and sublittoral zones are recognized as being particularly vulnerable to various sea-derived contaminants, such as nutrients, spilled oil, and organic pollutants (e.g., PCBs) (Brownawell and Farrington, 1986; Geng et al., 2021b; Slomp and Van Cappellen, 2004; Wu et al., 2015). The interactions between seawater and groundwater in coastal zones facilitate the deposition and penetration of these contaminants into beach environments. In this paper, we illustrate for the first time the diverse role of heterogeneous capillarity in the transport of solutes within swash zones, taking into account the combined impacts of waves and evaporation. Heterogeneous capillarity creates moisture hotspots that retain salt beneath the swash zone. These hotspots persist over tidal cycles due to capillary tension and the formation of capillary barriers at the boundaries of fine and coarser sediments. However, as evaporation occurs, salt begins to accumulate near the beach surface. The resulting hypersalinity creates vertical density gradients, leading to the downward migration of solutes through the unsaturated zone via the connected high capillarity zones where hydraulic conductivity is relatively higher compared to surrounding areas. In contrast, as solutes migrate into the saturated zone, they are predominantly transported along high-permeability-induced preferential flow pathways where sediment capillarity is low. Additionally, recursive seawater inundation and infiltration driven by oceanic forces (e.g., tides and waves) often reset the near-surface salinity back to the seawater level, rendering these driving mechanisms periodic. Compared to each individual processes, combined driving processes create more dynamic changes in groundwater flow and salinity in coastal beach sediments. These findings suggest that the spatially heterogeneous moisture distributions and associated moisture hotspots can have substantially lasting effects on the persistence and transport of various soluble chemicals and contaminants within coastal beach sediments.

This study provides valuable insights into the complex interactions between wave action, evaporation, and sediment heterogeneity on groundwater flow and salinity dynamics in coastal swash zones. However, several limitations should be acknowledged. While the numerical simulations are informed by field data from previous studies, comprehensive model validation was limited due to the scarcity of field data, particularly concerning the exchange of water flow and chemical fluxes across the land–ocean-atmosphere interfaces. The highly dynamic nature of these processes, especially the influence of tides, waves, evaporation, and local heterogeneity, is challenging to capture through discrete sampling points, and the numerical model may not fully represent these complexities. Additionally, our study does not account for a wide range of coastal settings, beach sedimentary processes (such as erosion and accretion), or diverse meteorological conditions (such as rainfall), which could affect the generalizability of the findings. Future research could aim to incorporate these broader factors and validate the model with more extensive datasets, including high-resolution temporal and spatial measurements of flow and transport processes across the interfaces between land, ocean and atmosphere in coastal zones, to enhance the robustness and applicability of the results.

5. Conclusion

Simulations of moisture and salinity dynamics in the swash zone reveal that wave action increases near-surface moisture, leading to a higher evaporation rate, characterized by dynamic fluctuations due to high-frequency surface inundation driven by swash motion. Heterogeneous capillarity creates localized moisture hotspots that support evaporation and salt accumulation, even when the overall moisture conditions along the swash zone are not conducive to evaporation, thus significantly raising salinity levels in these areas. Capillary barriers formed during swash infiltration allow moisture hotspots to persist across tidal cycles, trapping saltwater pockets within unsaturated sediments. These moisture hotspots in high-capillarity zones create preferential pathways, allowing evaporation-induced hypersaline water to penetrate deeper into saturated sediments. These insights are crucial for enhancing our understanding of coastal groundwater flow, biogeochemical conditions, and the resulting nutrient cycling and contaminant transport in coastal zones. They underscore the necessity of considering integrated coastal physical drivers when investigating coastal flow and transport processes in coastal swash zones.

CRediT authorship contribution statement

Xiaolong Geng: Writing – original draft, Validation, Methodology, Funding acquisition, Conceptualization. **Holly A. Michael:** Writing – review & editing, Validation, Methodology, Funding acquisition. **James W. Heiss:** Writing – review & editing. **Michel C. Boufadel:** Methodology, Funding acquisition, Conceptualization. **Hailong Li:** Resources, Formal analysis, Conceptualization. **Yan Zhang:** Writing – review & editing, Methodology.

Declaration of competing interest

The authors declare that they have no known competing financial interests or personal relationships that could have appeared to influence the work reported in this paper.

Acknowledgments

This work was funded by the US NSF (EAR2130595 and CBET2345629). However, it does not necessarily reflect the views of the funding agency, and no official endorsement should be inferred.

Appendix A. Supplementary data

Supplementary data to this article can be found online at https://doi.org/10.1016/j.jhydrol.2024.132322.

Data availability

Data will be made available on request.

References

Abou Khalil, C., Prince, V.L., Prince, R.C., Greer, C.W., Lee, K., Zhang, B., Boufadel, M.C., 2020. Occurrence and biodegradation of hydrocarbons at high salinities. Science of the Total Environment 143165.

Adams, E.E., Gelhar, L.W., 1992. Field study of dispersion in a heterogeneous aquifer: 2. Spatial Moments Analysis. Water Resour. Res. 28, 3293–3307.

Armonies, W., 1988. Physical factors influencing active emergence of meiofauna from boreal intertidal sediment. Marine Ecology Progress Series. Oldendorf 49, 277–286.

Bakhtyar, R., Brovelli, A., Barry, D.A., Li, L., 2011. Wave-induced water table fluctuations, sediment transport and beach profile change: Modeling and comparison with large-scale laboratory experiments. Coast. Eng. 58, 103–118.

Boufadel, M.C., Suidan, M.T., Venosa, A.D., 1999. A numerical model for density-and-viscosity-dependent flows in two-dimensional variably saturated porous media. J. Contam. Hydrol. 37, 1–20.

Boufadel, M.C., Lu, S., Molz, F.J., Lavallee, D., 2000. Multifractal scaling of the intrinsic permeability. Water Resour. Res. 36, 3211–3222.

Brownawell, B.J., Farrington, J.W., 1986. Biogeochemistry of PCBs in interstitial waters of a coastal marine sediment. Geochim. Cosmochim. Acta 50, 157–169.

Cassman, K., Munns, D., 1980. Nitrogen mineralization as affected by soil moisture, temperature, and depth. Soil Sci. Soc. Am. J. 44, 1233–1237.

Castle, J.W., Molz, F.J., Lu, S., Dinwiddie, C.L., 2004. Sedimentology and fractal-based analysis of permeability data, John Henry member, Straight Cliffs formation (upper Cretaceous), Utah, USA. J. Sediment. Res. 74, 270–284.

Chambers, L.G., Guevara, R., Boyer, J.N., Troxler, T.G., Davis, S.E., 2016. Effects of salinity and inundation on microbial community structure and function in a mangrove peat soil. Wetlands 36, 361–371.

Dagan, G., 2012. Flow and transport in porous formations. Springer Science & Business Media.

Dentz, M., Le Borgne, T., Englert, A., Bijeljic, B., 2011. Mixing, spreading and reaction in heterogeneous media: A brief review. J. Contam. Hydrol. 120, 1–17.

Einav, R., Harussi, K., Perry, D., 2003. The footprint of the desalination processes on the environment. Desalination 152, 141–154.

Elfrink, B., Baldock, T., 2002. Hydrodynamics and sediment transport in the swash zone: a review and perspectives. Coast. Eng. 45, 149–167.

Gallagher, E., Wadman, H., McNinch, J., Reniers, A., Koktas, M., 2016. A Conceptual Model for Spatial Grain Size Variability on the Surface of and within Beaches. JMSE 4, 38. https://doi.org/10.3390/jmse4020038.

Gelhar, L.W., 1993. Stochastic Subsurface Hydrology. Prentice-Hall, Englewood Cliffs, New Jersey.

Geng, X., Boufadel, M.C., 2015a. Impacts of evaporation on subsurface flow and salt accumulation in a tidally influenced beach. Water Resour. Res. 51, 5547–5565.

Geng, X., Boufadel, M.C., Xia, Y., Li, H., Zhao, L., Jackson, N.L., Miller, R.S., 2014. Numerical study of wave effects on groundwater flow and solute transport in a laboratory beach. J. Contam. Hydrol. 165, 37–52.

Geng, X., Boufadel, M.C., 2015b. Numerical modeling of water flow and salt transport in bare saline soil subjected to evaporation. J. Hydrol. 524, 427–438.

Geng, X., Boufadel, M.C., 2015c. Numerical study of solute transport in shallow beach aquifers subjected to waves and tides. J. Geophys. Res. Oceans 120, 1409–1428.

Geng, X., Boufadel, M.C., Jackson, N.L., 2016. Evidence of salt accumulation in beach intertidal zone due to evaporation. Sci. Rep. 6, 31486. https://doi.org/10.1038/srep31486.

Geng, X., Boufadel, M.C., 2017. The influence of evaporation and rainfall on supratidal groundwater dynamics and salinity structure in a sandy beach. Water Resour. Res. 53, 6218–6238.

Geng, X., Heiss, J.W., Michael, H.A., Boufadel, M.C., 2017. Subsurface flow and moisture dynamics in response to swash motions: Effects of beach hydraulic conductivity and capillarity. Water Resour. Res. 53, 10317–10335.

Geng, X., Boufadel, M.C., Rajaram, H., Cui, F., Lee, K., An, C., 2020a. Numerical study of solute transport in heterogeneous beach aquifers subjected to tides. Water Resour. Res. 56.

Geng, X., Heiss, J.W., Michael, H.A., Boufadel, M.C., Lee, K., 2020b. Groundwater flow and moisture dynamics in the swash zone: effects of heterogeneous hydraulic conductivity and capillarity. Water Resour. Res. 56. https://doi.org/10.1029/2020WR028401.

Geng, X., Michael, H.A., Boufadel, M.C., Molz, F.J., Gerges, F., Lee, K., 2020c. Heterogeneity affects intertidal flow topology in coastal beach aquifers. Geophys. Res. Lett. 47.

Geng, X., Heiss, J.W., Michael, H.A., Li, H., Raubenheimer, B., Boufadel, M.C., 2021a. Geochemical fluxes in sandy beach aquifers: Modulation due to major physical stressors, geologic heterogeneity, and nearshore morphology. Earth Sci. Rev. 221, 103800.

Geng, X., Khalil, C.A., Prince, R.C., Lee, K., An, C., Boufadel, M.C., 2021b. Hypersaline Pore Water in Gulf of Mexico Beaches Prevented Efficient Biodegradation of Deepwater Horizon Beached Oil. Environ. Sci. Tech. https://doi.org/10.1021/acs.est.1c02760.

Geng, X., Boufadel, M.C., Li, H., Na Nagara, V., Lee, K., 2023. Impacts of Evaporation-Induced Groundwater Upwelling on Mixing Dynamics in Shallow Wetlands. Geophys. Res. Lett. 50. https://doi.org/10.1029/2023GL104642.

Grattieri, M., Minteer, S.D., 2018. Microbial fuel cells in saline and hypersaline environments: Advancements, challenges and future perspectives. Bioelectrochemistry 120, 127–137. https://doi.org/10.1016/j.bioelechem.2017.12.004.

Guntiñas, M.E., Leirós, M., Trasar-Cepeda, C., Gil-Sotres, F., 2012. Effects of moisture and temperature on net soil nitrogen mineralization: A laboratory study. Eur. J. Soil Biol. 48, 73–80.

Heiss, J., Michael, H., Koneshloo, M., 2020. Denitrification hotspots in intertidal mixing zones linked to geologic heterogeneity. Environ. Res. Lett.

Heiss, J.W., Ullman, W.J., Michael, H.A., 2014. Swash zone moisture dynamics and unsaturated infiltration in two sandy beach aquifers. Estuar. Coast. Shelf Sci. 143, 20–31.

Heiss, J.W., Puleo, J.A., Ullman, W.J., Michael, H.A., 2015. Coupled surface-subsurface hydrologic measurements reveal infiltration, recharge, and discharge dynamics across the swash zone of a sandy beach. Water Resour. Res. 51, 8834–8853.

Heiss, J.W., Post, V.E., Laattoe, T., Russoniello, C.J., Michael, H.A., 2017. Physical controls on biogeochemical processes in intertidal zones of beach aquifers. Water Resour. Res. 53, 9225–9244.

Hirt, C.W., Nichols, B.D., 1981. Volume of fluid (VOF) method for the dynamics of free boundaries. J. Comput. Phys. 39, 201–225.

Horn, D.P., 2006. Measurements and modelling of beach groundwater flow in the swash-zone: a review. Cont. Shelf Res. 26, 622–652.

Jia, J., Bai, J., Gao, H., Wang, W., Yin, S., Wang, D., Han, L., 2019. Effects of salinity and moisture on sediment net nitrogen mineralization in salt marshes of a Chinese estuary. Chemosphere 228, 174–182.

Lew, S., Glińska-Lewczuk, K., Burandt, P., Kulesza, K., Kobus, S., Obolewski, K., 2022. Salinity as a determinant structuring microbial communities in coastal lakes. Int. J. Environ. Res. Public Health 19, 4592.

Li, H., Li, L., Lockington, D., 2005. Aeration for plant root respiration in a tidal marsh. Water Resour. Res. 41.

Li, H., Boufadel, M.C., Weaver, J.W., 2008a. Tide-induced seawater–groundwater circulation in shallow beach aquifers. J. Hydrol. 352, 211–224.

Li, L., Steefel, C.I., Yang, L., 2008b. Scale dependence of mineral dissolution rates within single pores and fractures. Geochim. Cosmochim. Acta 72, 360–377.

Liu, Y., Zhang, C., Liu, X., Li, C., Sheuermann, A., Xin, P., Li, L., Lockington, D.A., 2022. Salt transport under tide and evaporation in a subtropical wetland: Field monitoring and numerical simulation. Water Resour. Res. 58.

Lu, C., Chen, Y., Zhang, C., Luo, J., 2013. Steady-state freshwater–seawater mixing zone in stratified coastal aquifers. J. Hydrol. 505, 24–34.

Mahfouf, J., Noilhan, J., 1991. Comparative study of various formulations of evaporations from bare soil using in situ data. J. Appl. Meteorol. 30, 1354–1365.

Malott, S., O'Carroll, D.M., Robinson, C.E., 2016. Dynamic groundwater flows and geochemistry in a sandy nearshore aquifer over a wave event. Water Resour. Res. 52, 5248–5264.

Nabavi, S.M.B., Miri, M., Doustshenas, B., Safahieh, A.R., Loghmani, M., 2013. Effects of a brine discharge over bottom polychaeta community structure in Chabahar bay. Journal of Life Sciences 7, 302.

Neal, A., Pontee, N.I., Pye, K., Richards, J., 2002. Internal structure of mixed-sand-and-gravel beach deposits revealed using ground-penetrating radar. Sedimentology 49, 789–804. https://doi.org/10.1046/j.1365-3091.2002.00468.x.

Olorunsaye, O., Heiss, J.W., 2024. Stability of Saltwater-Freshwater Mixing Zones in Beach Aquifers With Geologic Heterogeneity. Water Resour. Res. 60. https://doi.org/10.1029/2023WR036056.

Oren, A., 2008. Microbial life at high salt concentrations: phylogenetic and metabolic diversity. Saline Systems 4, 2. https://doi.org/10.1186/1746-1448-4-2.

Paerl, H.W., Yannarell, A.C., 2010. Environmental dynamics, community structure and function in a hypersaline microbial mat. Modern and ancient microorganisms in stratified systems, Microbial mats, pp. 421–442.

Pecknold, S., Lovejoy, S., Schertzer, D., Hooge, C., Malouin, J., 1993. The simulation of universal multifractals. Presented at the Cellular Automata 228–267.

Peitgen, H.-O., Saupe, D., 1988. The science of fractal images. Springer-Verlag, New York Inc.

Robinson, C., Xin, P., Li, L., Barry, D.A., 2014. Groundwater flow and salt transport in a subterranean estuary driven by intensified wave conditions. Water Resour. Res. 50, 165–181.

Schertzer, D., Lovejoy, S., 1987. Physical modeling and analysis of rain and clouds by anisotropic scaling multiplicative processes. J. Geophys. Res. Atmos. 92, 9693–9714.

Sebben, M.L., Werner, A.D., 2016. A modelling investigation of solute transport in permeable porous media containing a discrete preferential flow feature. Adv. Water Resour. 94, 307–317.

Şen, H., 2005. Incubation of European Squid (Loligo vulgaris Lamarck, 1798) eggs at different salinities. Aquac. Res. 36, 876–881.

Silvestri, S., Defina, A., Marani, M., 2005. Tidal regime, salinity and salt marsh plant zonation. Estuar. Coast. Shelf Sci. 62, 119–130.

Slomp, C.P., Van Cappellen, P., 2004. Nutrient inputs to the coastal ocean through submarine groundwater discharge: controls and potential impact. J. Hydrol. 295, 64–86.

Sous, D., Lambert, A., Rey, V., Michallet, H., 2013. Swash–groundwater dynamics in a sandy beach laboratory experiment. Coast. Eng. 80, 122–136.

Sous, D., Petitjean, L., Bouchette, F., Rey, V., Meulé, S., Sabatier, F., Martins, K., 2016. Field evidence of swash groundwater circulation in the microtidal rousty beach, France. Adv. Water Resour. 97, 144–155.

von Jeetze, P.J., Zarebanadkouki, M., Carminati, A., 2020. Spatial heterogeneity enables higher root water uptake in dry soil but protracts water stress after transpiration decline: A numerical study. Water Resour. Res. 56.

Wang, T., Zhang, K., Li, H., Zheng, Y., Luo, M., Zeng, Z., Yu, S., Shen, C., Jiao, J.J., 2023. Multiple Seepage-Faces in Tidal Flat With Very Gentle Slopes. Geophys. Res. Lett. 50.

Weeks, S.W., Sposito, G., 1998. Mixing and stretching efficiency in steady and unsteady groundwater flows. Water Resour. Res. 34, 3315–3322.

Wilcox, D.C., 1993. Turbulence modeling. DCW Industries.

Wilcox, D.C., 1998. Turbulence modeling for CFD. DCW industries La Canada, CA.

Wilson, A.M., Gardner, L.R., 2006. Tidally driven groundwater flow and solute exchange in a marsh: numerical simulations. Water Resour. Res. 42.

Wu, C., Zhu, H., Luo, Y., Teng, Y., Song, J., Chen, M., 2015. Levels and potential health hazards of PCBs in shallow groundwater of an e-waste recycling area, China. Environ. Earth Sci. 74, 4431–4438.

Xin, P., Robinson, C., Li, L., Barry, D.A., Bakhtyar, R., 2010. Effects of wave forcing on a subterranean estuary. Water Resour. Res. 46.

Xin, P., Zhou, T., Lu, C., Shen, C., Zhang, C., D'Alpaos, A., Li, L., 2017. Combined effects of tides, evaporation and rainfall on the soil conditions in an intertidal creek-marsh system. Adv. Water Resour. 103, 1–15.

Yannarell, A.C., Paerl, H.W., 2007. Effects of salinity and light on organic carbon and nitrogen uptake in a hypersaline microbial mat. FEMS Microbiol. Ecol. 62, 345–353.

Zeppilli, D., Leduc, D., Fontanier, C., Fontaneto, D., Fuchs, S., Gooday, A.J., Goineau, A., Ingels, J., Ivanenko, V.N., Kristensen, R.M., 2018. Characteristics of meiofauna in extreme marine ecosystems: a review. Mar. Biodivers. 48, 35–71.

Zhang, C., Li, L., Lockington, D., 2014. Numerical study of evaporation-induced salt accumulation and precipitation in bare saline soils: Mechanism and feedback. Water Resour. Res. 50, 8084–8106.

Zhang, J., Lu, C., Shen, C., Zhang, C., Kong, J., Li, L., 2021. Effects of a low-permeability layer on unstable flow pattern and land-sourced solute transport in coastal aquifers. J. Hydrol. 598, 126397. https://doi.org/10.1016/j.jhydrol.2021.126397.